

STUDY OF THE DEFORMATION OF COMPRESSOR BLADES DURING ROTATING STALL

Taher Halawa

Mech. Engineering. Dept., Cairo Univ., Giza, 12316, Egypt
 Mechanical Engineering Department, UBC-University of
 British Columbia, Vancouver, B.C., V6T 1Z4, Canada
 E-mail: taherhalawa@yahoo.com

Dr. Osama Badr

Professor and Head,
 Mechanical Engineering Department,
 French University in Egypt (UFE),
 E-mail: osama.badr@ufe.edu.eg

Mohamed S. Gadala [Corresponding Author]

Mechanical Engineering Department, UBC-University of
 British Columbia, Vancouver, B.C., V6T 1Z4, Canada
 And: Abu Dhabi University, Abu Dhabi, UAE
 E-mail: gadala@mech.ubc.ca

Mohamed Y. AlQaradawi

Dept. of Mechanical and Industrial Engineering
 College of Engineering, Qatar University
 Email: myq@qu.edu.qa

NOMENCLATURE

d	Distance between fluid and structural meshes (m)
e	Element
F	Force (N)
K	Turbulence kinetic energy per unit mass (m^2/s^2)
M	Moment (N.m)
N	Node
R	Radial position (m)

Abbreviations

CFD	Computational Fluid Dynamics
DPIV	Digital Particle Imaging Velocimetry
FSI	Fluid-Structure Interaction
KSI	Kilo pound per Square Inch
NASA	National Aeronautics and Space Administration
NSE	Navier Stokes Equations
PSI	Pound per Square Inch
rpm	Revolutions per minute

Greek letters

ε	Turbulence dissipation rate (m^2/s^3)
---------------	---

Subscripts

x	x-direction
y	y-direction
z	Axial direction

ABSTRACT

This paper introduces aerodynamic simulations and structural analysis of a high speed centrifugal compressor at the stall condition. Simulations were performed for the compressor when the air injection control is applied and the results of the controlled compressor were compared to that for the uncontrolled compressor. The case of the compressor with air injection control was discussed in details in a previously published paper done by the authors of the current presented work. It was found that the stall effect is maximized at the impeller exit and at the vaneless area due to the strong pressure and velocity fluctuations resulting from the random

interaction between the main flow and the tip leakage flow. Results showed that the forces and moments for the controlled compressor case are lower than those for the uncontrolled compressor case during stall. Results showed also that the maximum deformation of the blades near the tip region is located at the area corresponding to end of the axial blade profile up to the start of radial blade profile.

1. INTRODUCTION

The instability caused by the rotating stall may damage the compressor blades because of the increased pressure fluctuations when the stall turns to surge [1].

There are two common types of stall; modes and spikes. Both of these types cause problems to the compressor blades but they have different way of appearance. The difference is that the modes are known to propagate in the axial direction with a long length scale while spikes propagate in the circumferential direction with finite amplitudes in a way much faster than the modes [2-4]. Vo et al. [5] explained the factors which can lead to rotating stall. It was found that when the tip leakage flow appears in the same time with a partial back flow through the vaneless region, the rotating stall initiates.

The compressor blades are affected by aerodynamic fluctuating forces during stall, and these forces cause relatively high deflection and stresses on the blades. For this reason, it is very important to study the effect of the unstable flow condition on the blades structure. For any aero elastic system, there are fluid and structure domains affecting each other. The fluid domain causes aerodynamic forces on the structure domain at which the stresses and deflections take place. The boundary movement between the two domains depends on the deformation and the reaction force in the same time. The coupling between the fluid and structure domains is known numerically as the Fluid-Structure Interaction (FSI).

The coupling between fluid and structure domains may be weak as for the turbo machinery flutter problems when the blades have a large inertia and the forces acting on it are relatively small [6]. For the case of small blade vibrations, the flow can be simulated by making a superposition of the steady

state flow and a small perturbation flow [7]. The nonlinear flow may result from the small blade vibrations if the operating flow condition is at the transonic region [8, 9].

Gnesin et al. [10] used the time marching method to simulate the blades vibration and the aero elastic action for an axial flow turbine. The mode shapes were combined linearly to represent the motion of the blades. Results showed that there is a nonlinear behavior due to the interaction between the mode shapes. This nonlinearity caused a limitation of the blade vibration oscillations. Srivastava et al. [11] made a numerical model based on solving the Navier Stokes Equations (NSE). The results of the model were compared to the results of other models which deal with a linearized potential flow equation and a linearized Euler equation in order to make the blade structural analysis for a turbine and for a fan. The comparison showed that the proposed model as well as the other models predicted the flutter mode and the inter blade phase angle with high accuracy. Also, it was found that the aerodynamic damping decreases as the back pressure increases. Im et al. [12] presented a numerical investigation about the causes of the non-synchronous vibration of axial compressor blades by making a coupled interaction between the fluid and structure domains. It was found that at the level of 78% of the span at the impeller leading edge, the vorticity and turbulence are very high and there are strong unstable tornado vortices which cause the vibrations of the blades. These tornado vortices are formed due to the complex flow resulted from the interaction between the main flow and the secondary flow including the tip clearance flow. Sadeghi and Liu [13] found that the flutter frequency at low mass flow rate is not the same as the blades natural frequency when using the coupled fluid-structure method, and this result is different from that for the uncoupled method for which the blades are assumed to oscillate at their natural frequencies.

The present paper focuses on the identification of the compressor blades deflection at the tip region during the development of stall to surge for a high speed centrifugal compressor. The most important point of this work is to check if the maximum blade deformation at surge exceeds the designed tip clearance value or not knowing that the existing compressor shroud surface was manufactured based on steady state structural analysis at an operating condition close to the surge limit. Blades deflections were also calculated for another case for which the air injection is applied at the vaneless region because it was found in a previous article published by the authors of the current paper that the air injection was able to stabilize the compressor when using specific injection parameters [14].

2. CASE STUDY

Figure 1 describes the configuration of the NASA CC3 centrifugal compressor which was selected in the present research. Figure 1 (a) shows the shape of the impeller and diffuser inside the compressor and Fig.1 (b) indicates the cross section view for all compressor components including the inlet guide duct, impeller, diffuser and the bend. The impeller of the NASA CC3 compressor is composed of 15 main blades and 15 splitter blades while the diffuser contains 24 vane-island

passages. The impeller has an inlet tip diameter of 210 mm and the diffuser exit diameter is 724 mm. This compressor is designed to deliver 4.54 kg/s at the best efficiency point with a total to static pressure ratio of 4 and this is corresponding to a rotational speed of 21,789 rpm. McKain and Holbrook [15] presented a complete view about the compressor specifications, geometry and structural analysis.

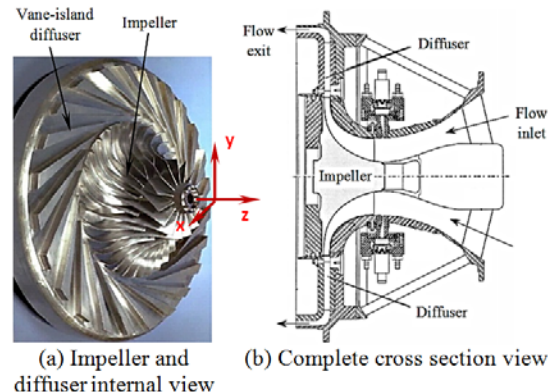


Figure 1. NASA CC3 compressor [16]

Controlling the rotating stall by using the air injection method for this compressor was discussed in previous studies [17, 18]. There are some studies presented various subjects concerning this compressor [16, 19-25]. The current paper discusses the structural analysis for the optimized air injection case reported in a previous study [14].

3. NUMERICAL ANALYSIS METHODOLOGY

The first part of the simulations was performed using FLUENT program [26] in order to find the air flow pressure and velocity distributions. For the second part, forces were transferred to a structural model in order to compute deflections and stress distribution by using APDL program [27].

For the CFD model, the density based method was used with second order discretization for space and time. The realizable K- ϵ turbulence model was applied as it can predict the high swirl flow behavior during surge accurately. The sliding mesh model [28] was selected to simulate the transient interaction between the impeller and diffuser. The pressure inlet and pressure outlet boundary conditions were set at the inlet and exit respectively because it was found that the solution converges with high accuracy in this way by fixing the pressure values at inlet and exit boundaries. Mesh sensitivity analysis was made in order to find the proper mesh with the highest possible quality by testing the mesh range between 5 and 16 million cells.

The process of increasing the number of CFD mesh elements was performed by taking into consideration decreasing of the cell mesh size near walls to maintain the dimensionless wall distance (Y-plus) in the suitable range of the turbulence model used as close as possible. The values of Y-plus were kept close to 30 at the blades tip region. The

values of Y-plus were set in the range from 30 to 300 at locations away from the first cell at wall.

For the purpose of achieving the solution temporal stability, the time step and the Courant number values were changed to find the most appropriate values that will make the solution stable. The solution reached the required level of convergence with using Courant number of 5 and time step of 4×10^{-6} second with performing 20 iterations per time step.

The cell orthogonal quality and the cell skewness were selected to show the degree of mesh quality as indicated in table 1. The average values as well as the standard deviation values are shown for the two mesh quality parameters.

Table1. Mesh quality parameters

Number of mesh elements	Cell orthogonal quality		Cell skewness	
	Average value	Standard deviation value	Average value	Standard deviation value
5 Million	0.75	0.095	0.3	0.15
7 Million	0.8	0.109	0.23	0.125
10 Million	0.83	0.115	0.22	0.123
12 Million	0.85	0.098	0.182	0.1
15 Million	0.85	0.092	0.15	0.11

It may be concluded from table 1 that when the number of mesh elements is increased, the orthogonal quality average value increases towards the value of 1, while the skewness average value decreases towards zero and this is a good indication about the mesh quality improvement. Also, the standard deviation values decrease as the number of mesh elements increases; this indicates how close the local values are to their mean.

Some flow parameters were monitored as the mesh density is changed in order to know solution accuracy. One of these parameters is the Mach number which is a very important parameter as it combines the variation effects of pressure and temperature. Figure 2 shows the Mach number variation with the mesh elements number at the compressor outlet. It may be noted from Fig.2 that the Mach number varies sharply in the beginning but this variation starts to approach zero when the number of mesh elements is increased above 10 million cells.

The same procedure of monitoring was done for other flow parameters and similar results were obtained about

the solution accuracy dependence on the mesh size. Based on the obtained results, the final selected number of CFD mesh elements was 14 million cells.

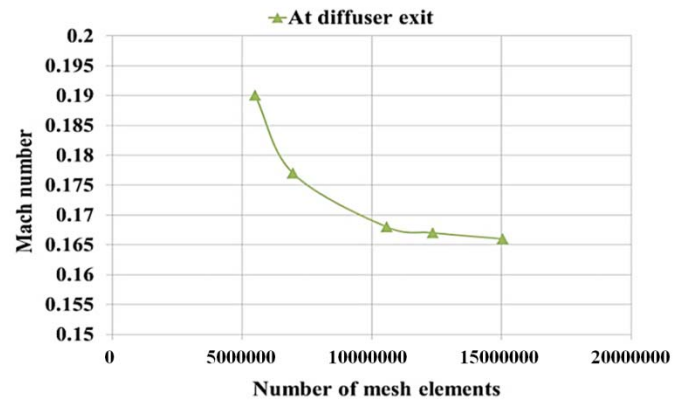


Figure 2. Mach number at compressor outlet for various mesh densities

The final selected CFD model mesh is about 15 million cells as shown in Fig. 3(a). More details about the mesh sensitivity analysis can be found in a previous published article [14].

For the mechanical model, the impeller solid volume was drawn and then meshed in a way that any small gap contains at least three mesh elements with a mesh growth rate of 1.2. Several trials were made to optimize the mesh quality by monitoring the mapped variables from the CFD mesh. The final mechanical model mesh is about 2 million cells as indicated in Fig. 3(b). The zero displacement boundary condition was applied at a specific location of the shaft near inlet. The same boundary condition was also applied at another location of the shaft near exit but this condition was not applied in the axial direction. The applied boundary conditions were assumed as mentioned in order to be matched with other boundary conditions used for a model done by NASA clarified in a technical report [15] for the purpose of validating the current model by comparing its results to that for the other model.

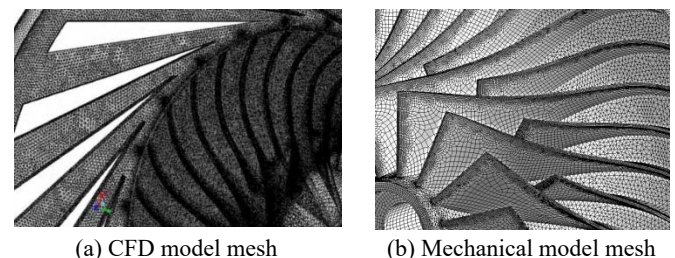


Figure 3. Mesh configurations

Forces were transmitted from the fluid domain to the structural domain across the meshes using the globally conservative interpolation method [28]. Each node on the fluid model mesh maps onto an element on the structural model

mesh and the transfer variable on the fluid model mesh is split into two components which are added to the structural model mesh nodes. The globally conservative interpolation method satisfies total force balance on the interface between the fluid and the structural model meshes. The mapping method used to transfer stresses from the fluid domain to the structural domain is the global algorithm [28]. At some locations, there is a gap between the two meshes; in this case, the node on the fluid mesh is mapped to the closest element on the structural mesh. Figure 4(a) shows that for the node N_1 , there are two facing elements e_1 and e_2 ; this node is mapped to the element e_1 because the distance d_1 is less than the distance d_2 , and this means that the selection criteria is based on minimizing the mapping transfer distance in the gap between the two meshes. In the case of that there is any misalignment between the interface edges, the mapping is done by selecting the closest node as shown in Fig. 4(b).

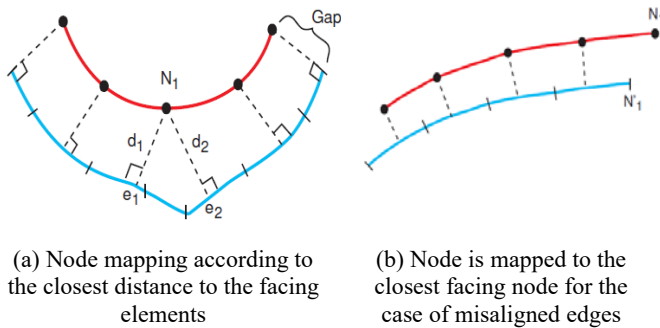


Figure 4. Global mapping method [28]

4. RESULTS

The results section is composed of three parts; the validation, CFD simulations and the structural analysis. In the validation part, the numerical model results are compared to other available experimental and numerical data provided from previous studies [15, 22]. The CFD simulations part contains the results obtained from the CFD model as the load acting on the blades during a period of time when the stall develops to surge. The structural analysis part shows the results extracted from the mechanical model including the deflections and stresses which were obtained after transferring the aerodynamic load from the CFD model.

4.1 Numerical Model Validation

The compressor pressure map was used for the validation of the CFD numerical model with the experimental data [22] as shown in Fig.5. The compressor map is composed of four curves; each curve represents a specific compressor rotational speed as a percentage of the design rotational speed which equals 21,789 rpm. For the numerical results, there are 6 to 7 different operating conditions were simulated to form each speed curve. The computational time

for each operating condition was about 10 hours by using computer capabilities of 16 cores, 2.1GHZ and 96 GB Memory and with taking into consideration that the time step used was 6×10^{-6} second. Figure 4 shows that the numerical model results are close to the experimental results with a relative error does not exceed 3 % which is a good indication that the model can provide accurate results for the aerodynamic simulations. Further validations for the CFD model were discussed in previous published articles [14, 29].

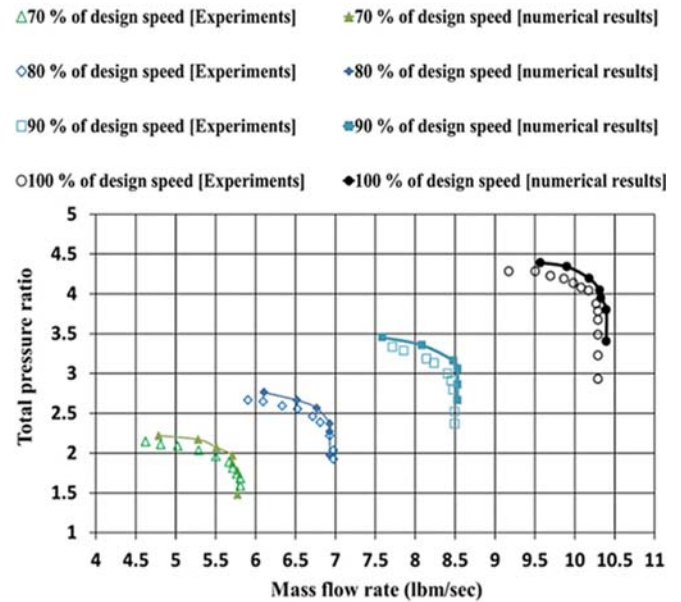
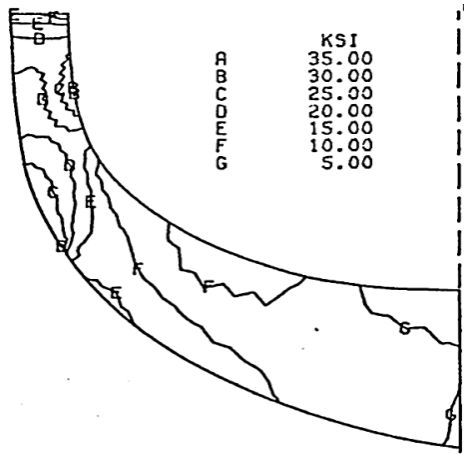
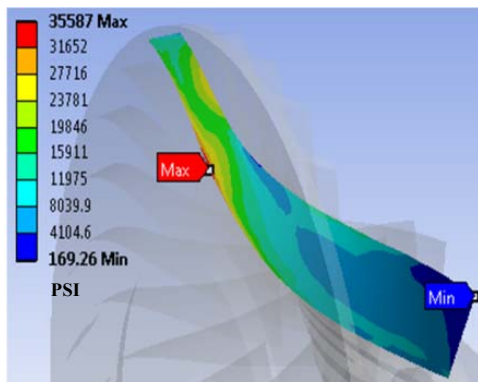


Figure 5. Compressor pressure map (numerical results versus measurements [22])

One of the most important parameters which are needed for the validation of the mechanical model is the stress distribution. Figure 6(a) shows the maximum principal stress at the full blade pressure surface for the numerical model results done by NASA [15]. The maximum principal stress at the full blade pressure surface for the results of the currently presented numerical model are presented in Fig.6 (b). By comparing Fig.6 (b) to Fig.6 (a), the currently presented numerical model results agree with the NASA model results that there are two regions with high stresses within the range from 27 KSI to 31 KSI at the hub and shroud surfaces close to the impeller exit and the location of the minimum stress is at the blade inlet.



(a) Maximum principal stress at the full blade pressure surface (according to NASA results [15])



(b) Maximum principal stress at the full blade pressure surface (according to the presented numerical model results)

Figure 6. Stress distribution at impeller blade surface for the presented numerical model and for the NASA numerical model results [15])

point and the corresponding stream lines show strong vortices with low velocity values. The third point is at the half way between stall and surge peak pressure while the fourth point is the at the surge peak pressure value. The stall regions at the third point become more powerful and some impeller passages are completely blocked as the stream lines show the vortices are shifted backward towards the impeller inlet in some passages. At the fourth point, the worst situation takes place because the stall areas are expanded and more impeller passages are blocked and a complete back flow occurs at this moment. This result makes the stall problem clearer that the blades deflection close to surge condition may be dangerous to the impeller at some points where the blades tip may touch the shroud surface.

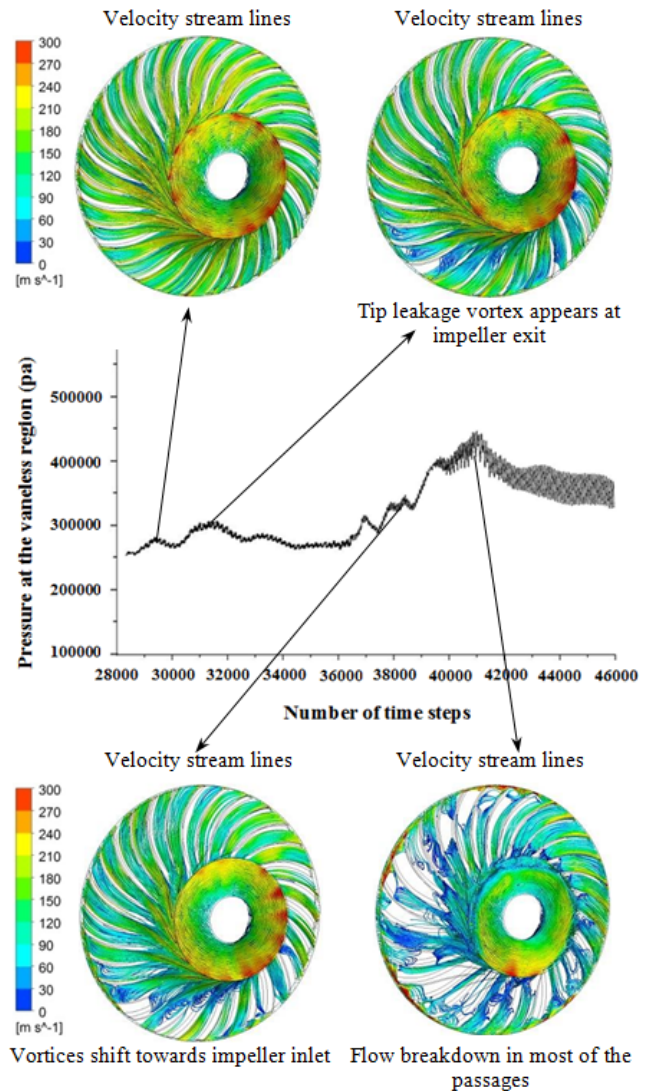


Figure 7. Pressure variation and velocity stream lines variation during stall development to surge

4.2 Monitoring Pressure and Velocity Variation at the Vaneless Region During Stall

The results obtained from the CFD model refer to that the maximum pressure fluctuations occur at the blades tip exit region including the vaneless space between the impeller and the diffuser. So, monitoring the flow variables at the vaneless space can show the maximum fluctuations with time. Figure 7 shows the pressure variation at the vaneless space with the number of time steps with the clarification of the velocity stream lines at some points on the pressure curve.

The points selected for reporting the stream lines represent the most effective variations of the flow from stall to surge. The first point is at the beginning of stall where there are some areas at the impeller exit with higher pressure values than the ideal ones. The stream lines are slightly disturbed with small interferences. At the second point, the amplitude of fluctuation is nearly doubled comparing with point 1. The high pressure areas are more intense than those for the previous

4.3 The Structural Analysis

The results in this section are presented in the form of comparisons between the original designed compressor (the uncontrolled compressor) and the compressor with using air injection (the controlled compressor). The air injection case used here was proved to keep the compressor aerodynamically stable at a mass flow rate of 3.8 kg/s or higher by using an air injection angle of 30 degrees [14].

4.3.1 Maximum principal stress variation near surge

At the steady state condition, the maximum principal stress and the equivalent stress distributions at the blades surface were discussed before as shown in Fig.6. During stall, these distributions vary strongly with time. For this reason, it was selected to show the peak value of these distributions during the transition from stall to surge. Figures 8 (a) and 8 (b) show the variation of the peak value of the maximum principal stress with time in rotor revolutions for the full blade and the splitter blade respectively.

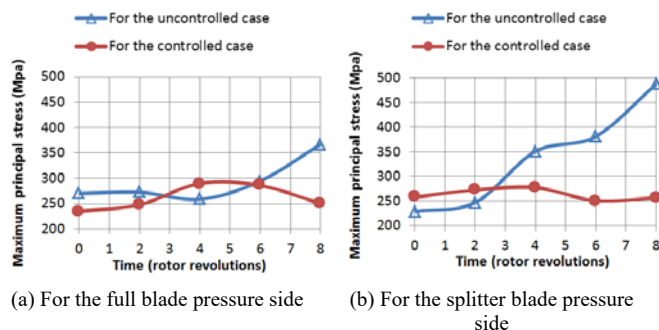


Figure 8. The variation of the peak value of the maximum principal stress with time for the impeller blade

The time frame shown in Fig.8 starts from a moment during stall (the reference time) up to the time corresponding to the peak of the first surge cycle. It may be seen from Fig.8 (a) that the maximum principal stress for the full blade for the two cases is fluctuating around two convergent mean values but there is some difference near the end because the final value of the uncontrolled case as it reaches 370 Mpa comparing with the final value of 250 Mpa for the controlled case. Fig.8 (b) shows that the stress distribution of the splitter blade for the uncontrolled case reaches relatively very high values up to 500 Mpa but the controlled case kept the same range of stress values for the full blade. This means that the controlled case is stable because both of the full and splitter blades have nearly the same stress range of variations. Finally, it may be concluded that for the uncontrolled case, there are stress fluctuations during stall and then the stress increases sharply when approaching surge but for the controlled case, the stress changes slightly with time and is more stable.

4.3.2 Force and moment variations near surge

The total force and moment were computed for the uncontrolled and controlled compressor cases in x, y and z directions. The z-direction represents the axial flow direction

while the x-y plane is perpendicular to z-direction, the x, y and z directions are clarified in Fig.1 (a). Figure 9 ((a) to (d)) shows the variation of F_x , M_x , F_y and M_y respectively with time for both of the controlled and the uncontrolled compressor cases. The time frame shown in Fig.9 is the same as explained before for Fig.8. Where F stands for the force and M represents the moment. There are strong fluctuations for F_x with time for the case of the uncontrolled compressor (Fig.9 (a)) and also the same thing for F_y (Fig.9 (c)); this is due to the non-uniform pressure distribution during stall as a result of the formation of stall cells at some impeller passages. Also, the mean fluctuation value is nearly zero for F_x variation which is a good indication that the compressor is balanced. The moment variation is a reflection of the fluctuations of the force magnitude and direction. For this reason, the M_x and M_y variations are close to zero for the controlled compressor case but they have relatively high values for the uncontrolled compressor case. In general, it may be concluded that the force and moment values are lower for the case with using air injection comparing with the uncontrolled compressor results.

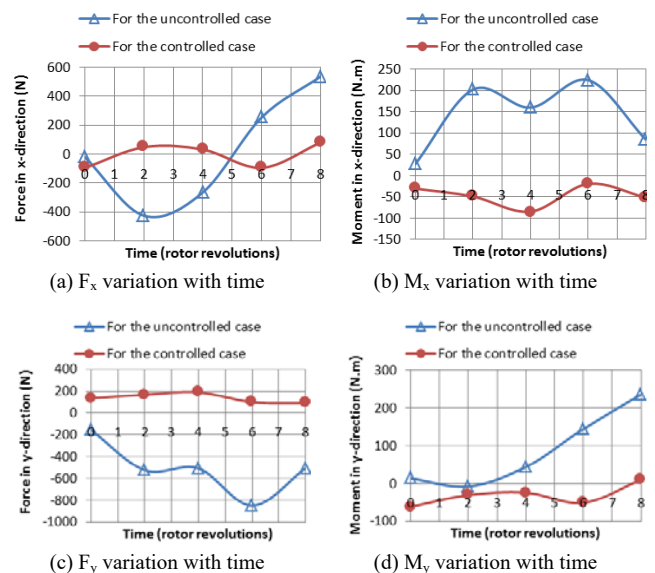


Figure 9. The variation of forces and moments with time

4.3.3 Deflection of the compressor blades during stall

The most important results are concerning the blades deflection especially at the blades tip zone because the compressor can be damaged if the deflection value is larger than the allowed tip clearance gap distance. Figure 10 (a) shows the full blades tip profile with maximum deformation which occurs at the peak pressure of the surge cycle for the uncontrolled compressor case. The base surface profile (before deformation) and the shroud surface profile are also shown in Fig.10 (a). The tip clearance value is relatively very small comparing with the complete axial distance Z and the radial distance R. For this reason, Fig.10 (a) does not show clearly the three profiles.

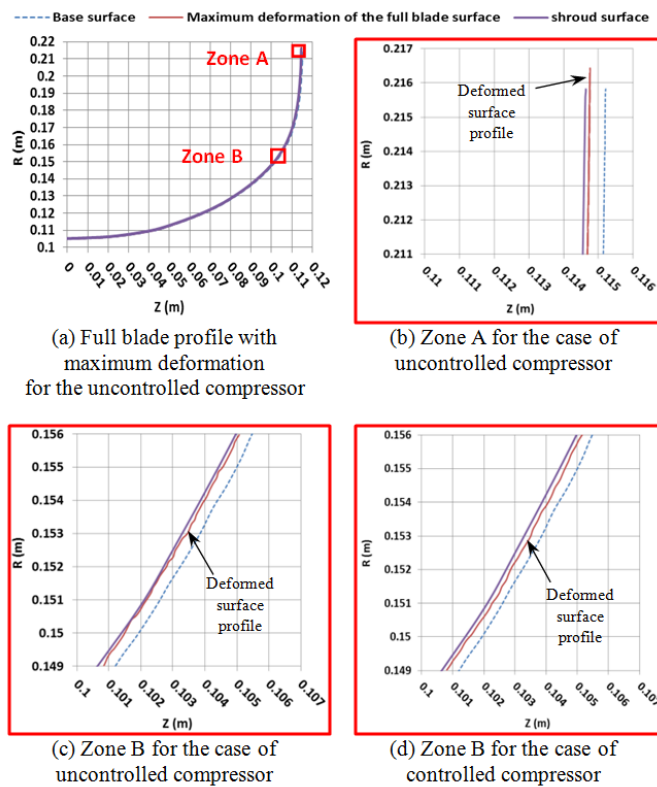


Figure 10. The maximum full tip blade surface deformation profile

Two zones were selected to show the deformation more clearly; these zones are named zone A and zone B. Zone A (Fig.10 (b) for the uncontrolled compressor case) is at the impeller exit. Zone B (Fig.10 (c) for the uncontrolled compressor case and Fig.10 (d) for the controlled compressor case) is at the transition from the axial to the radial profile. Actually the whole profile was checked for the deformation values but these zones were found to be the most critical areas where the deformed blade surface approaches the shroud surface. At zone A, the deformed full blade surface is close to the shroud surface but it does not touch it and also it may be noted from Fig.10 (b) that there is a deformation in the radial direction but it is not dangerous because it actually deforms freely in the vaneless region radially. At zone B, the deformed full blade surface approaches the shroud surface dangerously and touches it at some points at the z range from 0.1015 m to 0.103 m in Fig.10 (c). It was found also that for the splitter blade, the z range from 0.1017 m to 0.1028 m is a dangerous deflection zone. The reason for zone B to be the most critical deflection area is that at this region, the radial and axial deflection components are combined together and the resultant component direction is towards the shroud surface.

For the controlled compressor case (Fig.10 (d)), the results are much better than those for the uncontrolled compressor case (Fig.10 (c)) in terms of the maximum deformation values. By comparing the blade profile in Fig.10 (c) to that in Fig.10 (d), it may be noted that for the controlled compressor case, there is no touch between the blade surface and the shroud surface. This means that using the air injection

control was beneficial in decreasing the pressure fluctuations and hence decreasing the blade deformation during stall.

5. CONCLUSIONS

- The amplitude of the dynamic pressure fluctuations at blades tip increases with time as the stall develops to surge due to the interaction between the main flow and the secondary flow. The strongest fluctuations occur at the impeller tip exit due to the effect of reversed flow from diffuser during surge.
- At an operating condition close to surge, the compressor is exposed to high pressure fluctuations which affect the impeller blades and cause high stresses and deformation of the blades at the tip region.
- The compressor model with using air injection provides more stability than the uncontrolled compressor model in terms of minimizing the forces and moments variation with time during stall.
- The most critical part which has the maximum deformation was found to be at the blades tip area when the blades tip profile turns from axial to radial. The reason is that the radial and axial deflection components at this area are combined together and the resultant component direction is towards the shroud surface but for other areas as at the impeller inlet, the blade tip profile is axial, and so the axial deflection component is not effective.
- It is recommended to take into consideration the deflection calculations at the surge condition before the final manufacturing of the compressor. The reason is that it was found that the blades deflection during surge can cause compressor damage because the initial design for the tip clearance which is designed based on the steady state calculations is smaller than the deflection during surge at some locations.

ACKNOWLEDGMENTS

This publication was supported by NPRP grant No. 4-651-2-242 from the Qatar National Research Fund (a member of Qatar Foundation).

REFERENCES

- [1] Tan, C., Day, I., Morris, S., and Wadia, A., 2010, "Spike-type compressor stall inception, detection, and control," Annual review of fluid mechanics, 42, pp. 275-300.
- [2] Day, I., 1993, "Stall inception in axial flow compressors," Journal of Turbomachinery, 115(1), pp. 1-9.
- [3] McDougall, N. M., Cumpsty, N., and Hynes, T., 1990, "Stall inception in axial compressors," Journal of Turbomachinery, 112(1), pp. 116-123.
- [4] Paduano, J. D., Greitzer, E., and Epstein, A., 2001, "Compression system stability and active control," Annual review of fluid mechanics, 33(1), pp. 491-517.
- [5] Vo, H. D., Tan, C. S., and Greitzer, E. M., 2008, "Criteria for spike initiated rotating stall," Journal of Turbomachinery, 130(1).

- [6] Sadeghi, M., and Liu, F., "Coupled fluid-structure simulation for turbomachinery blade rows," Proc. 43rd AIAA Aerospace Sciences Meeting and Exhibit, pp. 2005-0018.
- [7] Clark, W. S., and Hall, K. C., "A time-linearized Navier-Stokes analysis of stall flutter," Proc. ASME 1999 International Gas Turbine and Aeroengine Congress and Exhibition, American Society of Mechanical Engineers, pp. V004T003A040-V004T003A040.
- [8] Carstens, V., and Belz, J., 2001, "Numerical investigation of nonlinear fluid-structure interaction in vibrating compressor blades," *Journal of Turbomachinery*, 123(2), pp. 402-408.
- [9] Johnston, D. A., Cross, C. J., and Wolff, J. M., 2005, "An architecture for fluid/structure interaction analysis of turbomachinery blading," AIAA paper no, 4013, pp. 10-13.
- [10] Gnesin, V., Rzakowski, R., and Kolodyazhnaya, L., 2000, "A Coupled Fluid-Structure Analysis for 3D Flutter in Turbomachines," *ASME J.*
- [11] Srivastava, R., Bakhle, M., Keith Jr, T., and Stefko, G., 2001, "Aeroelastic stability computations for turbomachinery."
- [12] Im, H.-S., and Zha, G.-C., "Simulation of non-synchronous blade vibration of an axial compressor using a fully coupled fluid/structure interaction," Proc. ASME Turbo Expo 2012: Turbine Technical Conference and Exposition, American Society of Mechanical Engineers, pp. 1395-1407.
- [13] Sadeghi, M., and Liu, F., 2005, "Computation of cascade flutter by uncoupled and coupled methods," *International Journal of Computational Fluid Dynamics*, 19(8), pp. 559-569.
- [14] Halawa, T., Gadala, M. S., Alqaradawi, M., and Badr, O., 2015, "Optimization of the Efficiency of Stall Control Using Air Injection for Centrifugal Compressors," *Journal of Engineering for Gas Turbines and Power*, 137(7), p. 072604.
- [15] McKain, T. F., and Holbrook, G. J., 1997, Coordinates for a high performance 4: 1 pressure ratio centrifugal compressor, National Aeronautics and Space Administration.
- [16] Skoch, G. J., 2000, "Centrifugal Compressor Flow Range Extension Using Diffuser Flow Control," NASA Glenn Research Center, Cleveland, Ohio, Dec, 5, p. 17.
- [17] Skoch, G., 2005, "Experimental Investigation of Diffuser Hub Injection to Improve Centrifugal Compressor Stability," *J Turbomach*(1), pp. 107-117.
- [18] Skoch, G. J., 2003, "Experimental investigation of centrifugal compressor stabilization techniques," *J Turbomach*, 125(4), pp. 704-713.
- [19] Chen, J.-P., Webster, R. S., Hathaway, M. D., Herrick, G. P., and Skoch, G. J., 2009, "High performance computing of compressor rotating stall and stall control," *Integrated Computer-Aided Engineering*, 16(1), pp. 75-89.
- [20] Halawa, T., Alqaradawi, M., Badr, O., and Gadala, M. S., "Numerical Simulation and Control of Rotating Stall in a Transonic Centrifugal Compressor," Proc. ASME 2014 12th Biennial Conference on Engineering Systems Design and Analysis, American Society of Mechanical Engineers, pp. V002T011A024-V002T011A024.
- [21] Halawa, T., Alqaradawi, M., Badr, O., and Gadala, M. S., "Numerical Investigation of Rotating Stall Characteristics and Active Stall Control in Centrifugal Compressors," Proc. ASME 2014 Power Conference, American Society of Mechanical Engineers, pp. V002T011A002-V002T011A002.
- [22] Skoch, G. J., Prahst, P., Wernet, M., Wood, J., and Strazisar, A., 1997, "Laser Anemometer Measurements of the Flow Field in a 4: 1 Pressure Ratio Centrifugal Impeller," DTIC Document.
- [23] Spakovszky, Z., 2004, "Backward Traveling Rotating Stall Waves in Centrifugal Compressors (2002-GT-30379)," *J Turbomach*(1), pp. 1-12.
- [24] Tarr, D. L., 2008, "Scaling of impeller response to impeller-diffuser interactions in centrifugal compressors," Massachusetts Institute of Technology.
- [25] Wernet, M. P., Bright, M. M., and Skoch, G. J., 2001, "An investigation of surge in a high-speed centrifugal compressor using digital PIV," *Transactions-American Society of Mechanical Engineers J Turbomach*, 123(2), pp. 418-428.
- [26] Fluent, A., 2011, "14.0," Userguide/Theoryguide.
- [27] APDL, A. M., 2012, "release 14.0," ANSYS Ltd.
- [28] ANSYS, R., 2011, "14.0, Help System," "Coupled Field Analysis Guide", ANSYS, Inc.
- [29] Halawa, T., Alqaradawi, M., Badr, O., and Gadala, M. S., "Numerical Investigation of Steady air Injection Flow to Control Rotating Stall in Centrifugal Compressors," Proc. ASME 2014 12th Biennial Conference on Engineering Systems Design and Analysis, American Society of Mechanical Engineers, pp. V002T011A025-V002T011A025.